The role of nanoclay in the generation of poly(ethylene terephthalate) fibers with improved modulus and tenacity

David W. Litchfield, Donald G. Baird*

Department of Chemical Engineering, Virginia Polytechnic Institute and State University, Blacksburg, Virginia 24061, United States

ARTICLE INFO

ABSTRACT

The effect of nanoclay concentration on the molecular orientation and drawability of poly(ethylene terephthalate) PET was examined using thermal and vibrational spectroscopic analysis. Although drawability at 83 °C in hot air increased by the addition of nanoclay, the maximum draw ratio was independent of nanoclay concentration. The average molecular orientation of the PET chain was found to mimic the trend in mechanical property improvements. Both Young's modulus and tenacity (i.e. strength) showed the maximum improvement at a 1 wt% loading of clay, which was shown to coincide with the maximum amount of molecular orientation. Nanoclay was shown to intercalate with PET and enhanced amorphous orientation that led to modulus and strength improvements. However, at higher concentrations of nanoclay the presence of large agglomerates prevented efficient orientation to the fiber axis and acted as stress concentrators to aid in cavitation and failure during testing. Raman spectroscopy showed that the as-spun unfilled PET fibers possessed significantly more *trans* rotamer content of the ethylene glycol moiety than the nanocomposite fibers.

© 2008 Elsevier Ltd. All rights reserved.

1. Introduction

The benefits of using layered silicate nanoparticles "nanoclays" for improving the physical, chemical, and mechanical properties of homogenous polymers have been shown by many studies [1–6] and reviewed by several authors [7–12]. These disk-shaped nanoparticles present a distinct advantage because significantly lower volume fractions are required to produce equal bulk property improvements when compared to conventional fillers (i.e. glass fibers, talc, etc.) [13]. The high specific surface area of nanoclay, due to its nanometer size and high aspect ratio, provides an increased number of polymer–particle and particle–particle interactions relative to conventional fillers. Maximum property improvements are believed to be obtained when the nanoparticles are uniformly dispersed into their individual sheets within the polymer matrix. Improvements in mechanical properties, for instance, have been widely cited for a number of polymer–nanoclay injection molded and, more recently, melt-spun fiber systems [9].

Several authors have reported the spinnability and mechanical properties of melt-spun nanocomposite fibers from polymer matrices of polypropylene [14,15], polyamide [16,17], and aromatic polyesters [18–24]. Nanocomposite fibers spun from isotactic polypropylene showed a significant reduction in tensile strength with increasing nanoclay concentration [14,15]. Using microscopy and thermal shrinkage measurements, the decrease in tensile strength was attributed to a loss of molecular orientation caused by crystallite growth perpendicular to the fiber axis during drawing [14,15]. Giza et al. [16] and Ibanes et al. [17] examined the effect of nanoclay on mechanical properties of polyamide-6 fibers with spinning speed and draw ratio, respectively. Values of modulus and tenacity were shown to increase with nanoclay concentration and spinning speed up to the onset of stress-induced crystallization [16]. Increasing the spinning speed beyond the point of stress-induced crystallization produced nanocomposite fibers with enhanced modulus but with reduced tenacity compared to unfilled polyamide-6 [16].

Ibanes et al. [17] showed that a 1 wt% loading of nanoclay in polyamide-6 fiber, spun to an un-oriented state and subsequently drawn above the glass transition, produced nanocomposite fibers with improved drawability. The tenacity and crystal orientation of the nanocomposite fibers were significantly increased relative to unfilled polyamide-6 fibers when drawn to their maximum draw ratios [17]. These authors showed little improvement in nano-composite fiber modulus and concluded that the nanoclay used did not interact favorably and couple with the oriented polyamide matrix. In addition, Ibanes et al. [17] did not examine the effect of nanoclay concentration on the degree of drawability or mechanical property improvement.

* Corresponding author. Tel.: +1 540 231 5998; fax: +1 540 231 2732.
  E-mail addresses: dlitchfi@vt.edu (D.W. Litchfield), dbaird@vt.edu (D.G. Baird).

Until recently [24] research on polyester nanocomposite fibers focused on modulus and tenacity improvements with spinning speed [18] or spinning speeds in the form of draw down ratios [19–23] and not on the effect of second step draw. McConnell et al. [18] showed that increasing the spinning speed enhanced both modulus and tenacity of poly(ethylene terephthalate) (PET) fibers at a given nanoclay loading and with a specific surfactant type. Chang et al. [19–23] examined several polyester nanocomposite systems at various draw down ratios from the spinneret. PET fibers filled with organically modified montmorillonite showed a decrease in modulus and tenacity with increasing draw down ratio, but the fiber properties improved overall with nanoclay addition at constant draw down [21]. In a more recent study, Chang et al. [23] found that modulus and tenacity were optimal at a 1 wt% addition of organically modified mica, but these properties were nearly independent of draw down ratio. The as-spun nanocomposite and pure PET fibers showed very low elongations at break (~3%) during loading at room temperature. In addition, the current literature [18,21,23] focusing on as-spun polyester nanocomposite fibers has shown modulus and tenacity values insufficient for industrial applications.

In our previous work [24], we reported good spinnability of nanocomposite fibers with alkyl surface-modified montmorillonite nanoclay concentrations below 5 wt%. Furthermore, significant increases were observed at low loadings of nanoclay in the modulus and tenacity of the nanocomposite fibers after drawing in a second step [24]. Table 1 summarizes the mechanical property improvements obtained from our previous study. For nanoclay loadings up to 1 wt%, the modulus improvement of the drawn nanocomposite fibers was observed to be much greater than a rule of mixtures prediction, which has not been reported in the prior nanocomposite fiber literature. As well, the tenacity of the nanocomposite fibers reached a maximum at the 1 wt% loading and was 66% greater than the tenacity of the unfilled PET fiber. Therefore, it was concluded that the PET phases in the neat and nanoparticle filled fibers possessed different morphologies. Additionally, the nanocomposite fibers showed increased drawability over the pure PET fiber. These observations were considerably different from those of previous authors examining PET nanocomposite fibers [18,21,23]. We concluded that solid state polymerization of the melt-compounded PET nanocomposites provides a means of keeping the molecular weight high enough to sustain axial loading over more strain units. Therefore, in the nanoclay filled fibers the orientation of the polymer chains was believed to be enhanced relative to unfilled PET.

The current literature on PET nanocomposite fibers has not fully explained the microstructure of these systems. Several authors [18,25–29] have cited that nanoclays act as nucleating agents in

PET, and those examining PET fibers have shown that nanoclay addition increases the degree of crystallinity of as-spun filaments [18]. Although some authors have reported property improvements, no studies of PET nanocomposite fibers have reported the effect of nanoclay on molecular orientation [18,21,23]. It is well known that increases in fiber tenacity depend upon the degree of orientation of the polymer chains, while the modulus of the fiber relies upon the degree of crystallinity and amorphous orientation [30]. Therefore, a complete understanding of the mechanism behind the property improvements attained with nanoclays requires knowledge of the inter-play between the four phases involved: the rigid nanoclays and the three phases of PET (crystalline, oriented-amorphous, and purely amorphous).

This work evaluates the role of nanoclay in creating property improvements in PET nanocomposite fibers after drawing in a second step above the glass transition temperature. In particular, this work examines how the presence of nanoclay leads to greater drawability and molecular orientation of the PET phase, and then correlates these observations to the improvements in mechanical properties. Wide angle X-ray (XRD) measurements were made to discern the effect of nanoclay dispersion on final nanocomposite properties. Thermal analysis by differential scanning calorimetry (DSC) and thermal shrinkage measurements was used to probe the effects of nanoclay on crystallinity and amorphous orientation, respectively. Raman spectroscopy was used to examine the changes in molecular conformations (i.e. *gauche–trans* isomerism) and also to study the changes in orientation of the PET backbone as a function of draw.

2. Experimental

2.1. Materials

The poly(ethylene terephthalate) used in this study had an intrinsic viscosity of 0.96 dl/g and was suitable for tire-cord applications. Surface-modified montmorillonite nanoclay Cloisite 20A was obtained from Southern Clay Products Inc (Gonzalez, TX) and used without further modification. The surface-modified clays are produced commercially by the substitution of interlayer sodium cations by dimethyl, bis(hydrogenated-tallow)quaternary ammonium cations.

2.2. Melt-compounding, fiber spinning, and fiber drawing

The production of the PET nanocomposite fibers was described in our previous work [24,31]. It is important to reiterate that the fiber spinning and drawing steps were performed separately in this work, but within a reasonable time frame to avoid complexity with physical aging. The draw oven was set to raise the temperature of the filaments to 83 °C, just above the glass transition temperature of PET. Maximum draw ratios were determined by increasing the speed ratio of the godets and observing the onset of fiber fraying (i.e. filament mechanical failure), upon which the speed was reduced slightly.

2.3. Characterization

The tensile properties of the nanocomposite fibers were determined using an Instron 4204 Universal Testing Machine at room temperature and humidity. A crosshead speed of 30 cm/min was used for testing the drawn fibers at a gauge length of 25.4 cm. For the un-oriented fibers, gauge lengths of 7.62 cm and crosshead speeds of 9.0 cm/min were used. Reported values are averages of 8 samples with uncertainties corresponding to 95% confidence limits.

The morphology of the nanoclay within the PET nanocomposites was determined using wide angle X-ray diffraction (XRD) and scanning electron microscopy (SEM). XRD patterns were obtained

Table 1
Tensile properties of PET/MMT nanocomposite fibers

Clay type	Nanoclay loading (wt%)	Draw ratio	M_w (g/mol)	Young's modulus (relative)	Maximum tenacity (relative)	Toughness (MPa)	Elongation at break (%)
Pure PET as-spun	0.0	–	45,800	1.00	1.00	197 ± 6.8	191 ± 8.9
Cloisite 20A as-spun	0.5	–	45,800	0.74	0.92	262 ± 15	284 ± 5.9
	1.0	–	44,900	0.83	1.10	277 ± 18	300 ± 3.1
	1.5	–	43,200	0.91	1.00	235 ± 5.4	279 ± 10
	3.0	–	38,800	0.74	0.57	190 ± 12	298 ± 19
Pure PET drawn	0.0	2.5	45,800	1.00	1.00	36.4 ± 2.8	6 ± 0.5
Cloisite 20A drawn	0.5	3.7	45,800	1.19	1.44	30.8 ± 2.8	5.6 ± 0.2
	1.0	3.5	44,900	1.28	1.63	29.4 ± 1.4	5.5 ± 0.2
	1.5	3.5	43,200	1.09	1.31	21.0 ± 1.4	5.1 ± 0.3
	3.0	3.6	38,800	0.94	0.95	18.2 ± 1.4	4.7 ± 0.3

using a Scintag XDS 2000 diffractometer with Cu K radiation at a wavelength of 1.54 Å with a scan rate of 0.5°/min from 1.5 to 10°. This study was not immediately focused on complete exfoliation of the nanoparticles, and thus transmission electron images of the nanocomposite were not taken for the specimens showing little to no peak in the XRD pattern. SEM images were taken using a LEO (Zeiss) 1550 high-performance Schottky field-emission SEM.

The crystallization and melting behaviors were determined by rheology using a Rheometric Mechanical Spectrometer (RMS-800) and by differential scanning calorimetry (DSC) using a TA Instruments Q1000 thermal analyzer, repectively. Rheological "cooling curves" were made by cooling the temperature of the nano-composite melt at a rate of 40 °C/min and recording the storage modulus, G'. A 25 mm cone and plate geometry was used with an inert atmosphere. Samples were dried for 24 h at 120 °C prior to testing. The DSC was calibrated using sapphire and indium standards. Test specimens of about 10 mg were cut and sealed in hermetic aluminum pans. All tests were carried out under a nitrogen atmosphere. Samples were heated from 40 °C to 290 °C, equilibrated for 5 min and cooled back to 40 °C, and then reheated to 290 °C. The heating and cooling rates were set at 20 °C/min. The degree of crystallinity was calculated under the assumption that the heat of fusion is proportional to the crystalline content, as shown in Eq. (1)

$$\chi = \frac{\Delta H_f}{\Delta H_f^o \left(1 - w_{clay}\right)} \tag{1}$$

where ΔH_f is the enthalpy of fusion of the sample, ΔH_f^o is the enthalpy of fusion of a completely crystalline sample and taken in this work as 140 J/g [32], and w_{clay} is the weight fraction of nanoclay in the nanocomposite fiber.

Thermal shrinkage measurements of the drawn nanocomposite fibers were obtained according to ASTM D4974-04 at 177 °C using 0.009 g per filament tex. The reported values are an average of 8 tests with uncertainties corresponding to 95% confidence limits.

Polarized Raman spectra were collected from a JY Horiba Lab-Ram HR spectrometer, with 600 groves/mm gratings and a slit width of 80 μm. Excitation was provided by a 632.8 nm Laser Physics 100S-632 HeNe laser. The laser was focused through a 40× objective on single filaments glued across the openings of 3/8 inch steel washers. Less than 10 mW of laser light was focused on the filaments. The detector was an electronically cooled open electrode CCD. Spectra were obtained from the samples in different geometrical arrangements using a rotating stage. In order to calculate the molecular orientation parameters, similar procedures of Lesko et al. [33] were followed. The detailed theory behind the determination of the molecular orientation parameters using polarized Raman spectroscopy is described elsewhere [33–37]. For the comparison of conformational isomers (*gauche* and *trans* content), the spectral bands were analyzed with the polarized light and fiber length arranged in parallel. Data analysis and peak fitting was done by using OriginPro v.8 (OriginLab) with embedded Gauss–Lorentz functions to deconvolute multiple peak bands and to determine the band full-width at half maximum (fwhm), peak center, and area. Accordingly, the area under the band was taken as the band intensity [35].

3. Results and discussion

3.1. Nanoparticle morphology

The wide angle X-ray diffraction (XRD) spectra of the series of as-spun PET nanocomposite fibers are shown in Fig. 1. The inset in Fig. 1 shows the pattern of pure Cloisite 20A as a reference for peaks
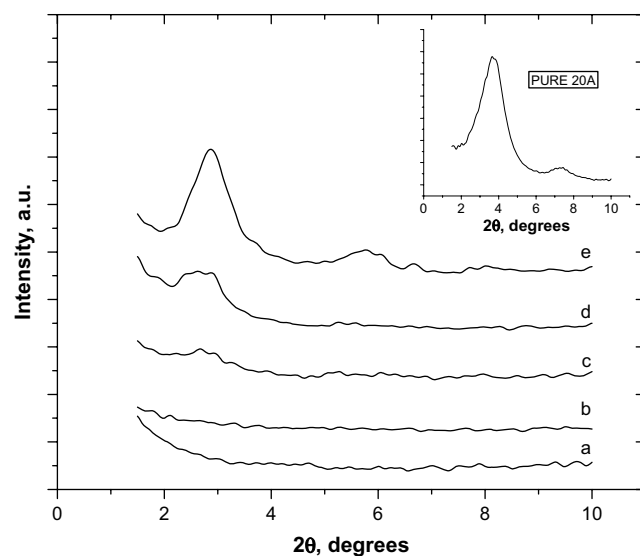

Fig. 1. XRD for the as-spun nanocomposite fibers (a) pure PET, (b) 0.5 wt% 20A, (c) 1 wt% 20A, (d) 1.5 wt% 20A, (e) 3 wt% 20A. Inset – pure Cloisite 20A nanoclay.

at 3.7° of 2θ, corresponding to the interparticle distance of organically modified clay, d_{001} or the "d-spacing", and 7.3° of 2θ, corresponding to a secondary peak, d_{002} [38]. The d-spacing from Bragg's law $(d_{001} = \lambda/2 \sin \theta)$, which corresponds to the interparticle distance, was shown to be 2.42 nm for the pure 20A nanoclay. For the as-spun fiber with various loadings of nanoclay, the peak height is very weak at low loadings. The peak position is shifted to slightly lower angles indicating that intercalation of PET into the nanoclay layers has occurred and the interparticle distance has increased. For nanoclay loadings below 3 wt%, the as-spun peak height is significantly suppressed, which implies that the number of agglomerates in the system is low. At 3 wt%, the large peak shows a pronounced number of aggregated nanoparticles in this fiber.

Fig. 2 shows the nanoparticle morphologies in the drawn fiber for various concentrations of 20A. Comparing the un-oriented and oriented fibers, the peak positions have been shifted to slightly higher angles and peak heights have been reduced. This indicates that drawing the nanoparticle fibers leads to a collapse in
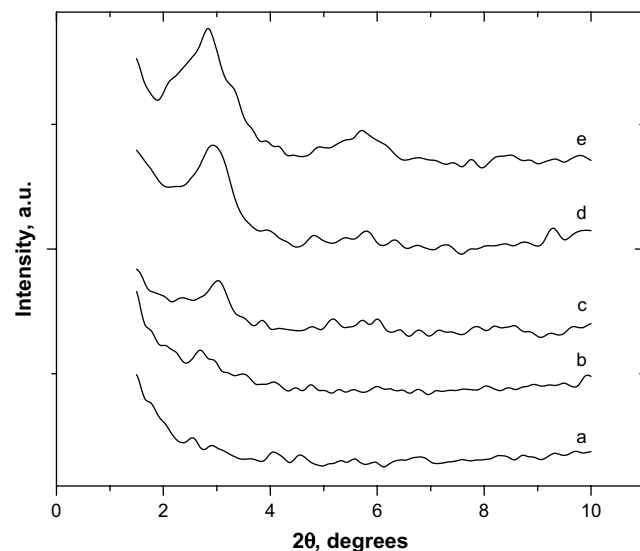

Fig. 2. XRD for the drawn nanocomposite fibers (a) pure PET, (b) 0.5 wt% 20A, (c) 1 wt% 20A, (d) 1.5 wt% 20A, (e) 3 wt% 20A.

interparticle distance. This collapse is suspected to be due to the reorganization of amorphous, curled polymer chains to oriented, extended chain crystallites. Although it appears that the particle spacings have collapsed, the number of stacked particles as agglomerates in the drawn nanocomposite fibers has decreased compared to the as-spun fibers. Thus, drawing has increased the aspect ratio of the stacks of nanoparticles and sheared the stacked agglomerates, so that the overlap of silicate layers has been reduced. Fig. 2 shows that the 1 wt% Cloisite 20A fiber undergoes the largest amount of collapse (~0.6 nm) compared to the 0.5, 1.5, and 3 wt% fibers after drawing. The number of agglomerated overlapping stacks increases monotonically with nanoclay concentration up to 3 wt%.

Scanning electron images of individual filament surfaces at the 3 wt% loading in the as-spun and drawn states are shown in Fig. 3a and b, respectively. Although the majority of the filament surface looks relatively smooth, as shown in Fig. 3c, distortions in the filament surface are observed every meter or so in the as-spun fiber at high loadings of nanoclay, and these are believed to be large agglomerates of nanoparticles. Interestingly, both operations of fiber spinning from the melt and fiber drawing in the solid state are not significantly disrupted by the presence of these distortions. Comparing Fig. 3a and b, it appears that drawing may elongate the agglomerates giving further support to the conclusions deduced from the XRD studies. However, from the standpoint of mechanical reinforcement, these elongated large agglomerates of nanoclay, seen only at the higher concentrations, are believed to act as points of stress concentrations and may lead to premature failure of the PET fiber. Yet, this does not explain for the increased drawability of these nanocomposites and a further examination into the morphology of the PET microstructure is given below.

3.2. Thermal behaviors

The ability to draw PET nanocomposites may depend upon the degree of crystallinity among other factors. DSC and rheological measurements were carried out to understand the role of 20A concentration on the crystallization process. Fig. 4 shows the DSC cooling behavior of PET nanocomposite melts at 20 °C/min. The 1.5 wt% sample has been omitted for clarity. Similar to other reports on the crystallization of PET nanocomposites [26,28,29], the presence of nanoclay increases the onset of crystallization and peak crystallization temperature relative to pure PET. However, it is clear that the addition of nanoclay has a limited effect. The onset of crystallization from the melt is increased by 3 °C at 0.5 wt% and by 5 °C at 1 wt% 20A, but at 3 wt% the shift in temperature has been reduced to 2 °C.

A similar trend is observed in the rheological cooling of the PET nanocomposite chips. Fig. 5 shows the build in complex viscosity, η^*, with temperature as the melt is cooled from equilibrium. The difference in onset temperatures is accentuated compared to the DSC measurement on the same nanocomposites. The onset of solidification is shifted 20 °C higher for the 1 wt% sample than the solidification temperatures of the other nanocomposites. It then appears by the rise in viscosity that the nanoparticles are immobilizing the polymer chains in the melt at higher temperatures. The nanoparticles themselves may also act as nucleating agents as cited by many authors [18,25–29].

Crystallization rates of two materials are typically compared by their time to reach 50% of the relative crystallinity, $t_{1/2}$ [39]. From non-isothermal measurements, such as those by DSC, the relative rate of crystallization may be determined by using Eq. (2) to define the relative degree of crystallinity, X, with temperature and by converting to the time domain through the cooling rate [40].
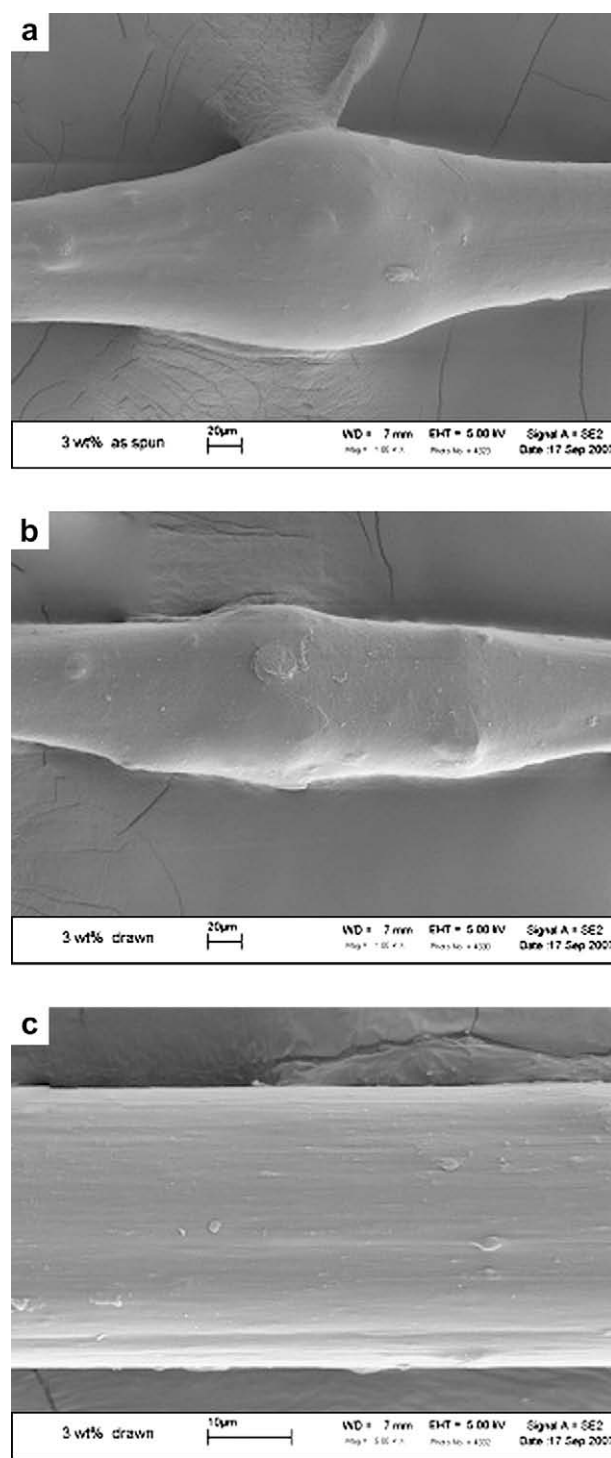
Fig. 3. SEM images of large agglomerates in the as-spun (a) and drawn, scale 20 mm (b) 3 wt% 20A nanocomposite fiber, scale 20 μm, and (c) a smooth section of the drawn fiber, scale 10 μm.

$$X = \int_{T_0}^{T} q\,\mathrm{d}T \bigg/ \int_{T_0}^{T_\infty} q\,\mathrm{d}T \qquad (2)$$

where T_0 and T_∞ are the onset and end of crystallization temperatures, respectively, and q is the heat flow at temperature T. Fig. 6 shows the difference in crystallization rates during non-isothermal cooling for the PET and PET nanocomposites. Interestingly, although the onset temperatures depend on the concentration of nanoparticles, the crystallization half times of the nanocomposites
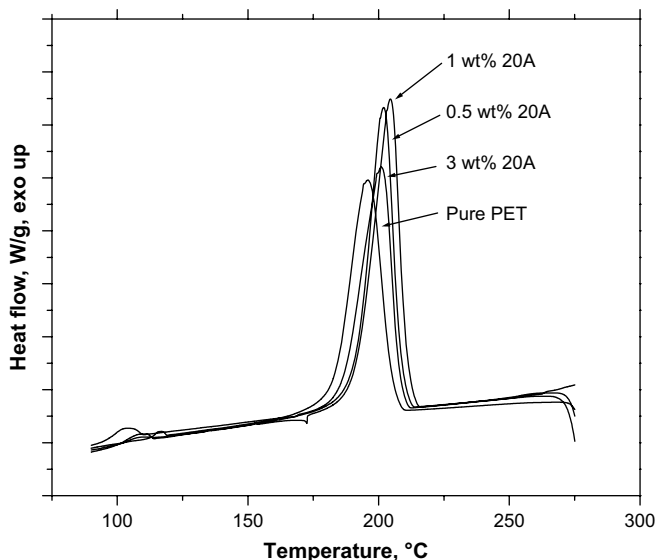
Fig. 4. Cooling from the melt at 20 °C/min, heat flow as a function of temperature for various nanoclay concentrations.

Fig. 6. Cooling from the melt at 20 °C/min, non-isothermal crystallization, X, as a function of time for various nanoclay loadings.

are independent of nanoclay loading. Additionally, the rate of crystallization is shown to improve when compared to the pure PET. Therefore, in terms of forming PET nanocomposites through non-isothermal processing operations, the degree of crystallinity in the nanocomposite samples is expected to be greater.

In our crystallization studies from the glassy state, e.g. when using the as-spun fiber, nanoparticles are not shown to induce crystallinity. In fact, Fig. 7 shows that the presence of nanoclay suppresses the non-isothermal crystallization of PET to higher temperatures. The onset of cold crystallization is shifted to higher temperatures in the nanocomposites. In the case of 0.5 and 3 wt% 20A the onset is 18 °C higher and at 1 wt% the onset temperature is 15 °C greater than that of the pure as-spun fiber. Although, the spinning speed for every sample was 550 m/min, it is believed that the pure fibers have some greater degree of pre-orientation or crystallinity that would nucleate cold crystallization at much lower temperatures than the nanocomposite samples. Yet, the non-isothermal crystallization rate, shown in Fig. 8, from the glassy state depends on the concentration of nanoclay. In the nanoclay filled
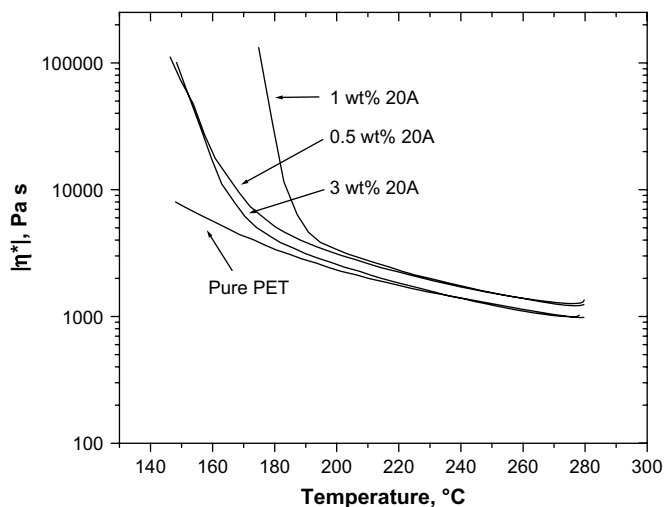
cases, cold crystallization progresses faster than the pure PET sample. Therefore, the crystal growth rate is accelerated by the presence of nanoclay and shifted to higher temperatures. The melting behavior of the as-spun nanocomposites and pure PET fibers are nearly equivalent with a slight shift (+2 °C) of the melting peak with the presence of nanoclay. In addition, within error the addition of nanoclay shows no significant effect on the glass transition, T_g, temperatures of PET, shown in Fig. 7 as 75 °C.

In the case of the drawn nanocomposite fibers, the thermal behavior during melting differs in the initial heat and repeated heating scans. Shown in Fig. 9 is the representative behavior during melting of the drawn pure PET, 1 wt%, and 3 wt% nanocomposite fibers. In the initial heating scan, the melting endotherms display shoulders at lower and higher temperature than the peak melting temperature reflecting a distribution of polymorphic crystalline structures in the fibers. The difference between the melting peaks of the 1st and 2nd heating scans decreases with increasing nano-clay concentration, possibly reflecting the reduced extended chain

Fig. 5. Complex viscosity as a function of temperature for the PET nanocomposite chips cooled at 40 °C/min, 100 rad/s, under nitrogen.

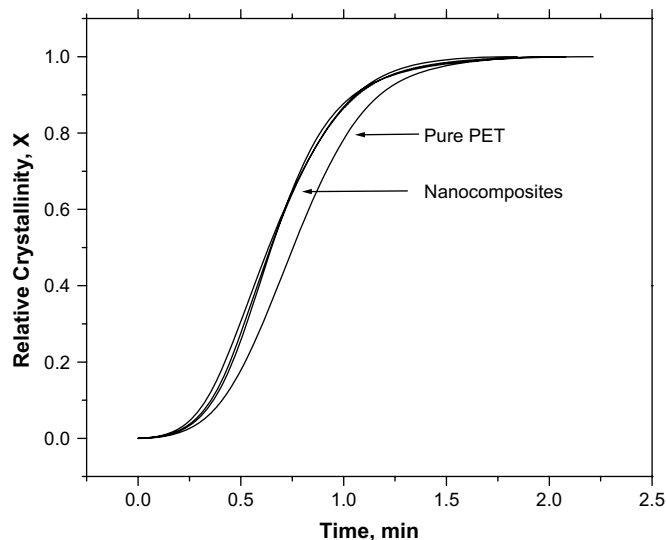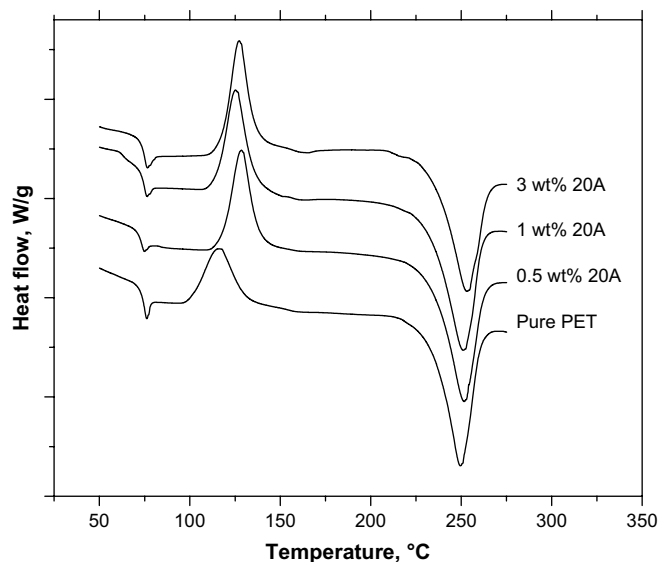
Fig. 7. 1st heating of the as-spun nanocomposite fibers at 20 °C/min, heat flow as a function of temperature for various nanoclay loadings (scaled for clarity).
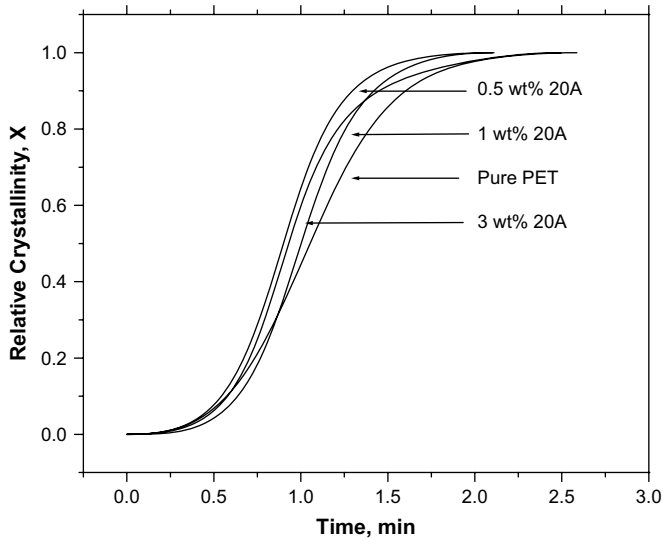
Fig. 8. 1st heating of the as-spun nanocomposite fibers at 20 °C/min, non-isothermal crystallization, X, as a function of time for various nanoclay loadings.

Table 2
PET nanocomposite fiber crystallinity, X_c, from DSC heating scans at 20 °C/min

Sample	X_c (%)
Pure PET as-spun	14.5
0.5 wt% 20A as-spun	10.1
1 wt% 20A as-spun	10.2
1.5 wt% 20A as-spun	9.7
3 wt% 20A as-spun	6.5
Pure PET drawn	37.4
0.5 wt% 20A drawn	36.6
1 wt% 20A drawn	35.5
1.5 wt% 20A drawn	34.2
3 wt% 20A drawn	32.2

crystalline morphology as nanoparticle concentration increases. PET crystallites at high loadings of nanoclay have a more chain folded structure.

By comparison of the melting enthalpy to the cold crystallization enthalpy in the drawn and as-spun cases, the degree of crystallinity, x_c, can be determined with nanoclay concentration. Table 2 shows that indeed the nanocomposite fibers have lower degrees of crystallinity than the pure PET fiber in the as-spun and drawn states. During melt spinning, the presence of the nanoclays alter the chain conformation of the PET chains either through particle–matrix interactions or through winding speed suppression due to the nanoclays' ability to dissipate some of the deformational energy in the spin-line. From the melt, the nanoclay particles form a temporary network structure with the PET chains preventing the development of crystalline order and amorphous orientation. The result of this type of interaction would also postpone stress-induced crystallization permitting the achievement of greater drawability.
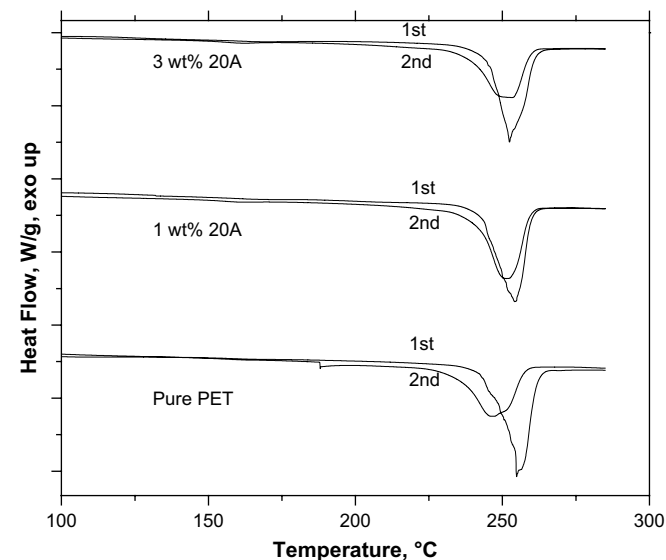
In terms of mechanical property improvements, the degree of crystallinity of the nanocomposites, as well as filler content, contribute to the level of stiffness. Table 2 shows that the drawn nanocomposite fibers have lower crystalline contents than the drawn pure PET fiber. Therefore, the observed improvement in Young's modulus as a function of nanoclay loading cannot be determined from crystallization data alone.

Thermal shrinkage experiments provide qualitative information on the degree of amorphous orientation in the PET and nanocomposite fibers [30]. The degree of thermal shrinkage expressed as the percent change in length of the filament after heating to 177 °C is shown in Fig. 10 for the drawn fibers. The addition of very low concentrations of nanoclay increases the degree of thermal shrinkage by 5% when the fibers have been drawn in a second step. Further addition of nanoclay has less of an effect, and at high loadings the degree of shrinkage is equivalent to that of pure PET fiber. Fiber strength and tenacity are dependent on the degree of molecular orientation [30], and the improvements observed here are qualitatively linked to the increased amorphous orientation (i.e. greater thermal shrinkage).

Q3

3.3. Molecular orientation and mechanical property improvement

Vibrational spectroscopic techniques are widely used non-destructive methods for the chemical and physical analyses of polymer molecules. Scattering methods, such as polarized Raman Spectroscopy, are powerful methods useful for determining molecular conformations, type and concentration of covalent
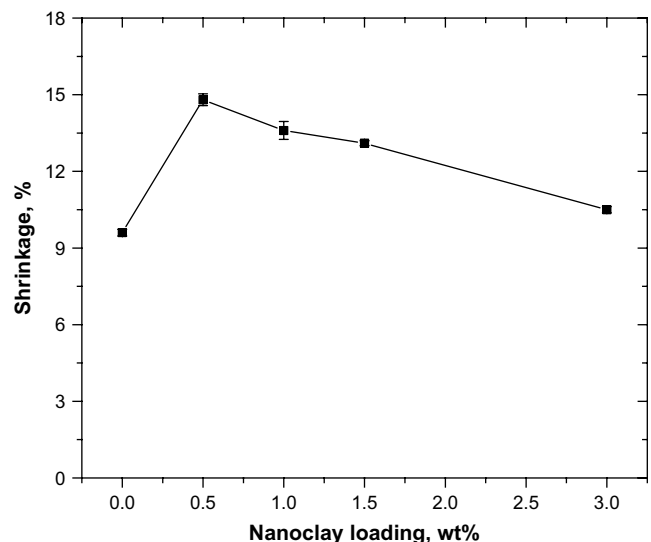

Fig. 9. 1st and 2nd heating of the drawn nanocomposite fibers at 20 °C/min, heat flow as a function of temperature for various nanoclay concentrations.

Fig. 10. Thermal shrinkage in percentage of the drawn nanocomposite fibers at 177 °C.

bonding, and molecular orientation of the polymer chain [41]. In brief, Raman scattering is the inelastic scattering of infrared light by a molecule upon returning to its lower energy level after an excitation. As the frequency of light is changed, various Raman active groups within the polymer sample vibrate and scatter light to produce bands of various intensities. When the light is polarized to a preferred direction of the electric field, an induced dipole moment in the molecule can occur. The interference of the scatter light with the incident polarized beam is analyzed to collect information on the orientation of these groups, for example with respect to the fiber axis. The theory of vibrational spectroscopy of PET has been outlined in more detail by Bower and Maddams [41] and others [33–35], and the advantages of using polarized Raman spectroscopy versus alternatives such as infrared, X-ray, and birefringence have been summarized by Tanaka and Young [36].

The Raman spectra of the as-spun PET nanocomposite fibers at 0, 1, and 3 wt% of alkyl modified nanoclay are shown in Fig. 11 for the range of 250–3250 cm^{-1}. The filaments are arranged parallel to the polarized light in this figure. Raman bands of interest for orientation or molecular conformation in as-spun and oriented pure PET are located at 998, 1095, 1130, 1180, 1281, 1310, 1616, and 1730 cm^{-1}. These bands and others have been assigned by Stokr et al. [42] and others [43] and are summarized in Table 3. Montmorillonite, MMT, has its own vibrational spectrum [44]. Characteristic bands for Na^+ MMT are mainly those related to Si–O vibrations and are located at 450, 710, 1100 cm^{-1} [44]. In Fig. 11b and c the bands at 1100 and 450 cm^{-1} are not present in the nanocomposite samples, and both the MMT SiO_4 tetrahedron and the PET C–C ring stretch contribute to the 700–710 cm^{-1} band. Yet, the number of scatterers in Raman spectroscopy is linearly proportional to the intensity of the band [41]. At the low weight fractions of nanoclay used in this study ($\leq$3%), the contribution of montmorillonite to the observed spectrum can be considered insignificant. Furthermore, Frost and Rintoul [44] observed that Raman spectra of MMT are difficult to obtain if the layers are dispersed or randomized in their spacing.

Nevertheless, the molecular conformations and orientation of the PET phase can be determined. Fig. 12 shows, by observation of the 1616 cm^{-1} band (phenylene ring stretch) in parallel and perpendicular arrangements to the polarized light, the absence of anisotropy from the as-spun 1 wt% 20A nanocomposite fibers and the presence of significant anisotropy in the drawn state of the

Table 3
Raman bands of interest for semicrystalline PET and montmorillonite

Wavenumber	Vibrational mode
450	SiO_4 stretching (MMT)
710	Ring C–C stretching
	SiO_4 stretching (MMT)
795	Ring torsion and C=O stretching
858	Ring C–C, ester CO–C
886	O–CH_2 and C–C stretch of the *gauche* ethylene glycol unit
998	O–CH_2 and C–C stretch of the *trans* ethylene glycol unit
1095	Ethylene glycol C–O and C–C stretching, C–O–C bending
1125	Ester CO–O and ethylene glycol C–C stretching
1180	Ring C–C stretching
1281	CO–C stretching
1310	Ring C–C stretching
1616	Ring C_1–C_4 stretching
1730	C=O stretching

same fiber. The drawn fibers thus show molecular orientation of the PET backbone to the fiber axis. The 1616 cm^{-1} band has been shown to be much less sensitive to changes in chain conformation (i.e. crystallinity), making it ideal for studying molecular deformation [43]. In addition when comparing Fig. 12a to b, the *trans* conformation of the ethylene glycol segments at 998 cm^{-1} shows anisotropy, indicating that there is some preferred crystalline orientation [35]. Discussed below, ideal crystallization converts *gauche* isomers to the all-*trans* conformation of the ethylene glycol moieties of the PET backbone [35]. The all-*trans* conformation of both the ethylene glycol and terephthalate units has been linked with the fully extended chain morphology that is desirable for high-performance PET fibers.

The molecular orientation coefficients determined from the second order Legendre polynomial (i.e. Hermans orientation function [36]), f_{1616} and f_{998}, of the system average backbone and ethylene glycol units, respectively, are shown in Fig. 13 for the
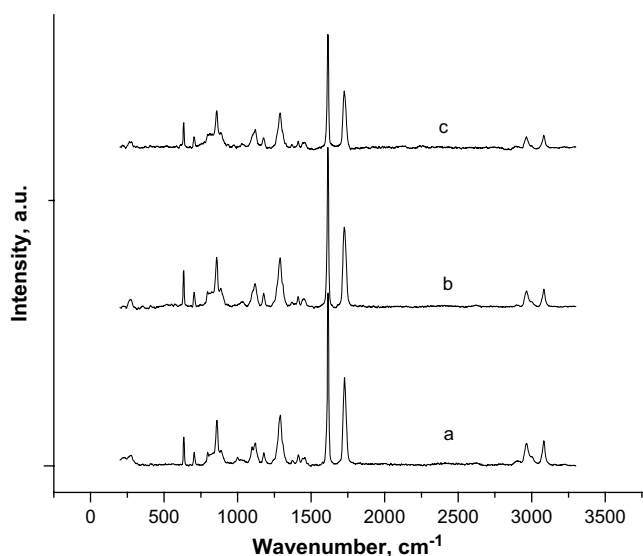

Fig. 11. Raman spectra of as-spun fibers of Pure PET (a), 1 wt% 20A (b), and 3 wt% 20A (c) with the fiber samples parallel to the vector of polarized light.
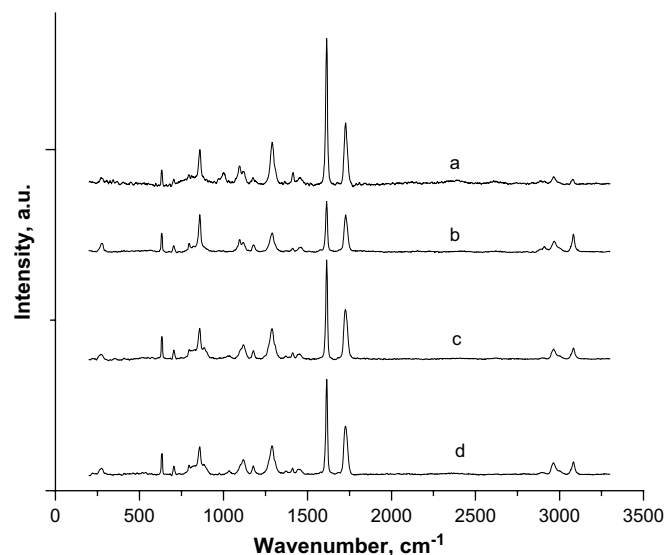

Fig. 12. Raman spectra of parallel and perpendicular arrangements of the wt% 20A as-spun and drawn fibers (a) parallel spectra of drawn 1 wt% 20A, (b) perpendicular spectrum of drawn 1 wt% 20A, (c) parallel spectra of as-spun 1 wt% 20A, (d) perpendicular spectrum of as-spun 1 wt% 20A.
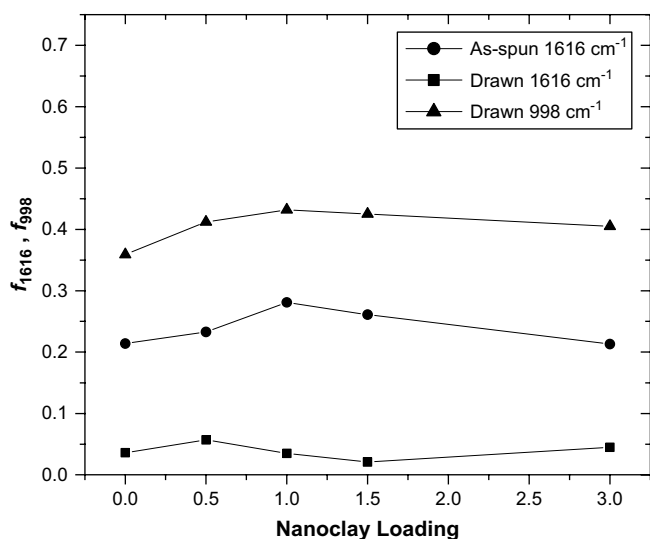
Fig. 13. Molecular orientation factor of the PET backbone (–C–C– stretch at 1616 cm^{-1}), f_{1616}, for the as-spun and drawn nanocomposite fibers and the orientation of the ethylene glycol units (stretch at 998 cm^{-1}), f_{998} for the drawn case only.

Fig. 14. 1727 cm^{-1} band as a function of nanoclay loading in the as-spun and drawn states, (a) Pure PET, (b) 1 wt% 20A, (c) 3 wt% 20A.

as-spun and drawn nanocomposite fibers. The f_{1616} and f_{998} are determined directly from the solution of the coupled non-linear algebraic equations outlined by Lesko et al. [33] and Yang and Michielsen [35] using 5 geometrical arrangements of the sample with respect to the incident polarized light. In the as-spun state, the average molecular orientation of the PET backbone is low, which is expected considering the relatively low winding speeds used during melt spinning. The nanocomposites do not possess a significant band at 998 cm^{-1} in the as-spun state and orientation coefficients calculated had large errors due to poor signal to noise resolution in our best spectra and are not displayed in Fig. 13. The drawn fiber backbone orientation coefficients show significant dependence on concentration of nanoclay. Both measures of orientation for the drawn fibers follow the trends in modulus and tenacity improvement with a maximum at 1 wt% of nanoclay. Beyond this loading, the orientation of the backbone and the crystalline units decreases with increasing nanoclay concentration. Yet, the reduction in crystal orientation is not as significant as that of the backbone. Therefore, low loadings of nanoclay may aid in the development of ordered polymer structures parallel to the fiber axis. High loadings may disrupt the long-range order because the polymer chains must organize themselves around a larger number of rigid particles. At low concentrations of nanoclay, the full benefit to orientation is not realized, as less nanoclay is available. Above the optimum nanoclay concentration, the reduced molecular orientation combined with the increased number of agglomerates that contribute to stress concentration reduces the fiber modulus and tenacity.

The orientation parameters observed in this study are relatively low compared to high-performance PET fibers and are most likely due to the low drawing speeds ($\sim$10 m/min). At low speeds, stress on the fiber is low and the development of stress-induced crystallization is delayed or absent. However, DSC measurements show the degree of crystallinity in the drawn fibers to be relatively high $\sim$40%. Yet, DSC overestimates the degree of crystallinity because the oriented-amorphous chains act as a precursor to thermal crystallization, as evidenced by the observation of thermal shrinkage. Through Raman spectroscopy, the carbonyl stretching band at 1727 cm^{-1} has been associated with sample density and crystallinity [33,45]. Fig. 14 shows that after drawing the full-width at half maximum, fwhm, (i.e. the fiber density) changes relatively little with respect to the as-spun fibers. Higher densities are associated with lower fwhm values and a corresponding shift in the peak to
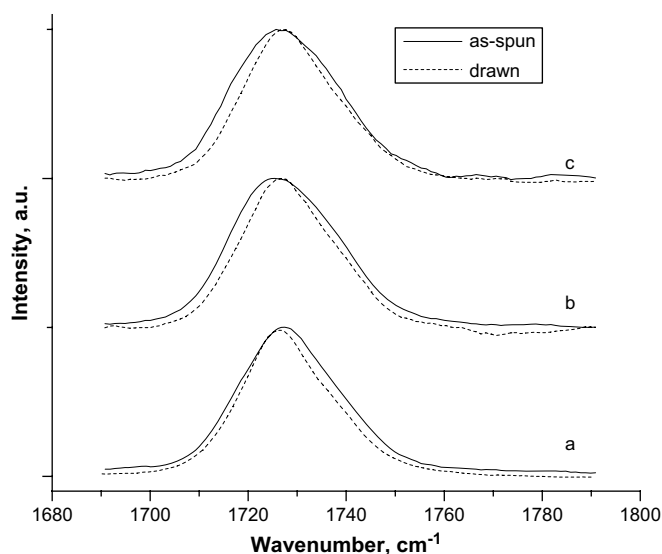
lower frequencies [45]. The 1727 cm^{-1} band has been regarded to provide insight into the conformation of the terephthalate group from *gauche* (at high fwhm) to *trans* (at low fwhm) [33]. Although the ethylene glycol units readily convert from *gauche* to *trans*, the terephthalate unit conformations remain relatively unaffected by drawing under these conditions. Thus, the *average* crystal and backbone orientations, which are the determined parameters via Raman spectroscopy, are low and the observed tenacity values are low compared to industry standards. However, compared to the current literature on PET nanocomposite fibers, the degree of mechanical property improvements listed in Table 1 has not been observed by others, particularly with regard to tenacity improvement. The effect of increasing drawing speed and stress-induced crystallinity is the subject of our on-going research.

3.4. Molecular conformation and drawability improvement

Interestingly, the nanocomposite fibers are capable of reaching higher draw ratios than the pure PET fiber. This is attributed to the effect nanoparticles have on the initial molecular conformation of the PET phase. As noted above, the *trans* conformation of the PET backbone is associated with extended chains, while the *gauche* conformation has been assigned to characterize chain folding and irregularity found in the amorphous phase. Fig. 15b–e shows the Raman spectra of the as-spun, low-orientation, PET nanocomposites in the range of 720–1550 cm^{-1} in comparison to the spectrum for pure PET (a) with the nanoclay filled fibers. The convoluted band in the range of 790–900 cm^{-1} is composed of four single bands at 795, 830, 858, and 886 cm^{-1}. As noted by others [46], the band intensity at 886 cm^{-1} can be compared with the 998 cm^{-1} band to determine the relative amounts of *trans* and *gauche* isomerism of the ethylene glycol units of the PET backbone. By visual inspection of Fig. 15a with b–e, it is clear that the pure PET sample has a larger content of the *trans* conformation than the nanoclay filled systems. Further evidence is provided by inspection of the 1050–1200 cm^{-1} range. A convoluted band near 1125 cm^{-1} is clearly split into two bands for the pure PET sample. The first peak at 1097 cm^{-1} has been assigned to the *trans* conformation of the amorphous or crystalline phase, while the second peak at 1130 cm^{-1} corresponds to the *gauche* isomerism of these phases. The nanoclay filled systems show only a shoulder at 1097 cm^{-1}, which reflects less *trans* content than the pure PET.
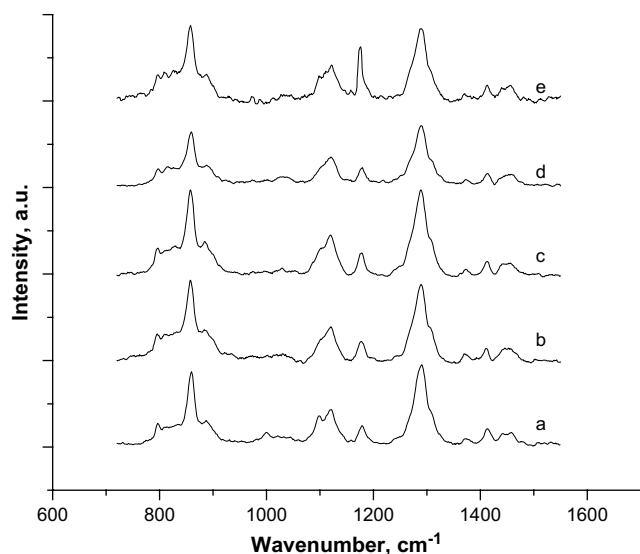
Fig. 15. Raman spectrum from 720 to 1550 cm^{-1} for the as-spun nanocomposite fibers, (a) pure PET, (b) 0.5 wt% 20A, (c) 1 wt% 20A, (d) 1.5 wt% 20A, (e) 3 wt% 20A.

Ibanes et al. [17] examined the drawability and orientation of only a 1 wt% loading of montmorillonite in polyamide-6. They found that nanoclay, indeed, increased drawability relative to unfilled polyamide, but did not lead to significantly enhanced molecular orientation when drawn to its maximum extent [17]. The authors deduced from small and wide angle X-ray measurements on the crystalline structure that the large impenetrable surfaces of the nanoclay block the development of inter-crystal tie chains, thereby reducing the entanglement density of the polyamide chain network [17].

For the PET nanocomposite fibers examined in this study a similar conclusion can be made for the increased extensibility of the polyester network. However, the effect of nanoclay concentration is considered here, as point of departure from the study of Ibanes et al. [17]. In Table 1 the maximum draw ratio is nearly independent of nanoclay loading. As nanoclay concentration is increased, the degree of agglomeration is increased as shown by the XRD peaks in Fig. 1. Therefore, the number of surfaces blocking entanglements remains relatively unchanged, because at higher concentrations the platelets are more likely to be stacked together into aggregates. If the platelets were exfoliated then perhaps higher draw ratios could be obtained as more entanglements are prevented with increased nanoclay concentrations up to a percolation limit. Additionally for the PET nanocomposite fibers, the nanocomposite samples have a less ordered structure after initial melt spinning than the pure PET. Therefore, the absence of crystallites, which have been shown to act as cross-link points between polymer chains, and lack of pre-orientation of the chains into their *trans* conformations permits the accomplishment of higher draw ratios with nanoclay filled PET fibers. The reduction in *trans* content is suggested to be the result of a combined effect of a favorable PET chain interaction with the silicate surface and the dissipation of deformational energy by the nanoclay during melt spinning.

To interpret the cause of the increased drawability and origin of the greater *gauche* content of the nanocomposite fibers a few of scenarios are worth considering. Similar trends with enhanced amorphous phase content in fibers have been observed for the melt spinning of polymer blends [47,48]. These authors concluded that because the primary phase produces a shear field around the filler phase, the elongational viscosity of the system is reduced, and the overall extension and orientation of chains is suppressed [47,48]. Polymer molecules tend to un-coil and then orient more readily

under stronger extensional flow. If the applied stress from the winding device is split between orienting the polymer molecules and the nanoparticles to the fiber axis, then the extensional flow can be considered weaker than if the whole stress was focused on the polymer chains alone.

An alternative explanation for the presence of an enhanced *gauche* content can be linked to PET–nanoclay surface bonding or "tetherment". From the intercalation data shown in Figs. 2 and 3 and from the modulus data of the drawn nanocomposites, some type of favorable coupling interaction is inferred between PET and the alkyl modified nanoclay. However, additional or abnormal bands in the Raman spectra of the nanocomposite fibers are not observed to any significance that would signify PET bonding with the surface of the nanoparticle or the surface treatment. For instance, surface hydroxyl groups on the montmorillonite nanoclay could bond with the ethylene glycol units on the PET chain, which would give rise to some change in the bands of O–C stretching. A bonded PET–nanofiller structure has been observed by Bikaris et al. [49] for silica filled PET, and a branched PET structure has been shown to lower the degree of crystallinity as well as broaden the melting endotherm in DSC experiments [50]. Although the nanocomposite degrees of crystallinity are reduced in the as-spun and drawn states relative to unfilled PET, the filled fibers have significantly increased drawability. Ibanes et al. [17] examined the drawability of polyamide-6 with hyperbranched fillers and a 1 wt% addition of montmorillonite. The hyperbranched additives significantly reduced drawability of PET by cross-linking the chains and restricting orientation development [17]. Therefore the rapid rise in complex viscosity of the nanocomposite resins, shown in Fig. 5, is probably not due to tetherment bonding of PET and nanoparticles. Instead it is more likely due to a combined effect of heterogeneous nucleation at the surface of the silicate and homogenous nucleation by the immobilization of polymer chains by the silicate layers. Both of these effects are dependent on the concentration and degree of dispersion of nanoclay. Therefore, the interaction between PET and alkyl modified nanoclay is considered favorable but rather weak, such that a well-connected PET–nanoclay network is not formed with these organically modified montmorillonites.

4. Conclusions

The role of alkyl modified montmorillonite in the improvement of PET fiber mechanical properties was discussed in terms of PET and nanoparticle morphology. When drawn to their maximum extents, modulus and tenacity improvement reached a maximum at a 1 wt% addition of nanoclay. Average molecular orientation of the phenylene rings and ethylene glycol groups reached a maximum with nanoclay concentration at 1 wt% as well. From thermal shrinkage measurements, the presence of nanoclay promoted the development of amorphous orientation. In addition, X-ray diffraction showed nanoparticle intercalation with PET, which suggested that favorable interaction existed between the polymer and nanoclay. At a 1 wt% loading of nanoclay, the degree of physical interaction with the polymer matrix yielded the optimal molecular orientation for the greatest amount of mechanical property improvement. For concentrations below 1 wt%, the loading of nanoclay was not high enough to develop significant interactions with PET and alter the extent of molecular orientation. The degree of parallel coupling of PET and nanoclay was below optimum due to the low concentration. Therefore, the modulus improvement was not as great as that with the 1 wt% loading. At concentrations above the optimum, the degree of nanoclay agglomeration increased, and we believe that the molecular orientation was disrupted by the inability of the polymer chains to efficiently rearrange around the larger stacks of particles parallel to the fiber axis. In addition, the larger agglomerates and the

increased presence of nanoclay aided in the dissipation of some of the deformation from the PET chains to the silicate stacks. Furthermore, at high concentrations the large agglomerates appear to act as stress concentrators. The combination of the above led to reduced mechanical properties at high nanoclay loadings.

The ability to obtain higher degrees of molecular orientation was linked to the increased drawability of the nanocomposite fibers relative to pure PET. Nanocomposite yarns can be drawn to a greater extent because of the larger *gauche* content of the ethylene glycol units that delay the orientation and subsequent crystallization of the PET chains to higher draw ratios. In the as-spun state for pure PET fiber, the degree of *trans* content may reflect pre-ordering of the polymer chains. The degree of *trans* content may also impart physical cross-links between ordered crystalline domains and serve as a nucleator for further crystallization. An increased amount of *gauche* content is due to a favorable, although weak, interaction with the silicate surface, such that the polymer chains remain in a predominantly coiled amorphous state. In addition, the nanoparticles themselves are able to dissipate some of the deformational energy from the spinning process. Therefore, there may be a suppression of effective winding speed, such that the polymer chains in the nanocomposite do not have the same as-spun ordering as the pure PET fibers at an equal spinning speed.

References

[1] Kojima Y, Usuki A, Kawasumi M, Okada A, Kurauchi T, Kamigaito O. J Appl Polym Sci Part A Polym Chem 1993;31:983–6.
[2] Messersmith PB, Giannelis EP. J Appl Polym Sci Part A Polym Chem 1995;33:1047–57.
[3] Gilman JW. Appl Clay Sci 1999;15:31–49.
[4] Fornes TD, Yoon PJ, Keskkula H, Paul DR. Polymer 2001;42:9929–40.
[5] Chu D, Nguyen QT, Baird DG. Polym Compos 2007;28:499–511.
[6] Nguyen QT, Baird DG. Polymer 2007;48:6923–33.
[7] Nguyen QT, Baird DG. Adv Polym Technol 2006;25:270–85.
[8] Ray SS, Okamoto M. Prog Polym Sci 2003;28:1539–641.
[9] Tjong SC. Mater Sci Eng Rev 2006;53:73–197.
[10] Giannelis EP. Adv Mater 1996;8:29–35.
[11] Litchfield DW, Baird DG. Rheol Rev 2006:1–60.
[12] Okada A, Usuki A. Macromol Mater Eng 2006;291:1449–76.
[13] Fornes TD, Paul DR. Polymer 2003;44:4993–5013.
[14] Houphouet-Boigny C, Plummer CJG, Wakeman MD, Manson J-AE. Polym Eng Sci 2007;47:1122–32.
[15] Pavlikova S, Thomann R, Reichert P, Mulhaupt R, Marcincin A, Borsig E. J Appl Polym Sci 2003;89:604–11.
[16] Giza E, Ito H, Kikutani T, Okui N. J Macromol Sci Phys 2000;B39:545–59.
[17] Ibanes C, David L, De Boissieu M, Seguela R, Epicier T, Robert G. J Polym Sci Part B Polym Phys 2004;42:3876–92.
[18] McConnell DC, Hornsby PR, Lew CY, Qua EH. Ann Tech Conf Soc Plastic Eng Tech Papers 2006:387–92.
[19] Chang JH, An YU, Kim SJ, Im S. Polymer 2003;44:5655–61.
[20] Chang JH, Kim SJ. Polym Bull 2004;52:289–96.
[21] Chang JH, Kim SJ, Joo YL, Im S. Polymer 2004;45:919–26.
[22] Chang JH, Mun MK, Lee IC. J Appl Polym Sci 2005;98:2009–16.
[23] Jung M-H, Chang J-H, Kim J-C. Polym Eng Sci 2007;47:1820–6.
[24] Litchfield DW. The manufacture and mechanical properties of PET fibers filled with organically modified MMT. Virginia Tech; 2008.
[25] Ke Y, Long C, Qi Z. J Appl Polym Sci 1999;71:1139–46.
[26] Phang IY, Pramoda K, Liu T, He C. Polym Int 2004;53:1282–9.
[27] Wang Y, Shen C, Li H, Li Q, Chen J. J Appl Polym Sci 2004;91:308–14.
[28] Wang Y, Gao J, Ma Y, Agarwal US. Compos Part B 2006;37:399–407.
[29] Calcagno CIW, Mariani CM, Teixeira SR, Mauler RS. Polymer 2007;48:966–74.
[30] Salem DR. Draw-induced structure development in flexible-chain polymers, Structure formation in polymeric fibers. Munich: Hanser; 2001.
[31] Baird DG, Litchfield DW, Rim PB. US Patent Appl 60/991550; 2007.
[32] Mehta A, Gaur U, Wunderlich B. J Polym Sci Polym Phys Ed 1978;16:289–96.
[33] Lesko CCC, Rabolt JF, Ikeda RM, Chase B, Kennedy A. J Mol Struct 2000;521:127–36.
[34] Citra MJ, Chase DB, Ikeda RM, Gardner KH. Macromolecules 1995;28:4007–12.
[35] Yang S, Michielsen S. Macromolecules 2002;35:10108–13.
[36] Tanaka M, Young RJ. J Mater Sci 2006;41:963–91.
[37] Bower DI. J Polym Sci Polym Phys Ed 1981;19:93–107.
[38] Southern-Clay-Products. Cloisite 20A: typical physical properties bulletin; 2008.
[39] van Krevelen DW. Properties of polymers. New York: Elsevier; 1990.
[40] Jeziorny A. Polymer 1978;19:1142.
[41] Bower DI, Maddams WF. The vibrational spectroscopy of polymers. Cambridge: Cambridge University Press; 1989.
[42] Stokr J, Schneider B, Doskocilova D, Lovy J, Sedlacek P. Polymer 1982;23:714–21.
[43] Yeh W-Y, Young RJ. J Macromol Sci Phys 1998;37:83–118.
[44] Frost RL, Rintoul L. Appl Clay Sci 1996;11:171–83.
[45] Melveger AJ. J Polym Sci Part A2 1972;10.
[46] Rodriguez-Cabello JC, Merino JC, Quintanilla L, Pastor JM. J Appl Polym Sci 1996;62:1953–64.
[47] Brody H. J Appl Polym Sci 1986;31:2753–68.
[48] Miles IS. J Appl Polym Sci 1987;34:2793–807.
[49] Bikiaris D, Karavelidis V, Karayannidis G. Macromol Rapid Commun 2006;27:1199–205.
[50] McKee MG, Unal S, Wilkes G, Long TE. Prog Polym Sci 2005;30:507–39.